

# Enhanced accuracy in 3D structured illumination microscopy through binary encoding with accelerated speed using sampling Moiré

Zhoumiao He<sup>a</sup>, Pei Zhou<sup>a,b</sup>, Jianwei Zhang<sup>a,b</sup>, Jiangping Zhu<sup>a,b,\*</sup>

<sup>a</sup> College of Computer Science, Sichuan University, Chengdu 610065, China

<sup>b</sup> National Key Laboratory of Fundamental Science on Synthetic Vision, Sichuan University, Chengdu 610065, China

## ARTICLE INFO

Dataset link: <https://github.com/abaowannasleep/structured-illumination-microscopy>

### Keywords:

SIM  
Fringe modulation  
Binary encoding  
Sampling Moiré

## ABSTRACT

Structured Illumination Microscopy (SIM) is widely recognized as a precise and stable technique for three-dimensional inspection. However, efficiently achieving precise results still poses a challenge to be addressed. This research paper presents significant advancements aimed at enhancing the precision and efficiency of the SIM system. We leverage the defocus sensitivity of binary fringes, which yields more accurate height mapping, reducing the error by an outstanding 5% to 20%. Additionally, we introduce a novel technique called sampling Moiré (SM) for modulation decoding from a single shot, resulting in a reduction of camera exposure time by  $(N - 1)/N$  compared to the N-step phase shift technique and a minimum 20% reduction in error compared to the Fourier transform (FT). These advancements elevate the system's precision and increase efficiency, making SIM an even more powerful tool for high-quality three-dimensional (3D) inspections.

## 1. Introduction

With the continuous advancement of the manufacturing industry, microdevices are being produced with ever-increasing precision, finding widespread applications in instrument processing, semiconductor manufacturing, and medical devices. The manufacturing accuracy of these microdevices plays a crucial role in determining their functionality and product quality, making three-dimensional surface inspection an essential aspect of industrial manufacturing [1,2]. As functional complexity increases, microdevice structures become more intricate, presenting challenges for inspecting their 3D surfaces. One specific challenge is signal obstruction and incomplete measurements caused by steep stages [3]. Over the past few decades, various methods have been developed to address this issue, including confocal scanning microscopy [4], interferometry [5], microdeflectometry [6], and SIM [7].

SIM has gained increasing attention in micro-structure measurement [8,9]. SIM recovers the sample topography by leveraging the influence of the object distance on fringe modulation within a limited depth of field (DoF) imaging system. Fringe modulation is determined using techniques such as the phase shift method [10] or FT [11]. The axial modulation response (AMR) curve indicates the modulation-sample height relationship. Identifying the curve's peak enables topographic reconstruction. Vogel et al. [12] made system modifications to ensure

identical curvatures of the object and projection shells as they pass through the same optical elements, optimizing SIM accuracy for varying specular and roughness levels [13]. Meng et al. [3] used light field imaging, estimating depth information from the epipolar plane image (EPI) of the light field. Zheng et al. [14] developed a theoretical signal formation model for smooth and rough surfaces.

Researchers aim to improve the speed and accuracy of measurement techniques, including SIM. In SIM, measurement speed depends on scanning speed and the required number of fringes for modulation extraction. Accuracy is influenced by systematic errors, modulation calculation precision, and modulation-height mapping accuracy. Yan et al. [15] used the modified weighted-gauss fitting algorithm (MWGFA) to enhance modulation-height mapping accuracy, but the algorithm is less efficient and requires further improvements. Lee et al. [16] introduced differential confocal microscopy (DCM) to eliminate scanning time by operating within the linear region of the axial modulation response (AMR). Lu et al. [17] projected vertical and horizontal sinusoidal fringes onto the sample and established a mapping relationship between fringe modulation ratio and actual position, but imperfect linearity in the linear region causes fitting errors. Xie et al. [18] developed a new differential SIM with an additional CCD camera to improve axial accuracy and resolution using a new response function derived from the subtraction and sum values of two AMRs. Han et al. [19] expanded on

\* Corresponding author at: College of Computer Science, Sichuan University, Chengdu 610065, China.

E-mail address: [zjp16@scu.edu.cn](mailto:zjp16@scu.edu.cn) (J. Zhu).

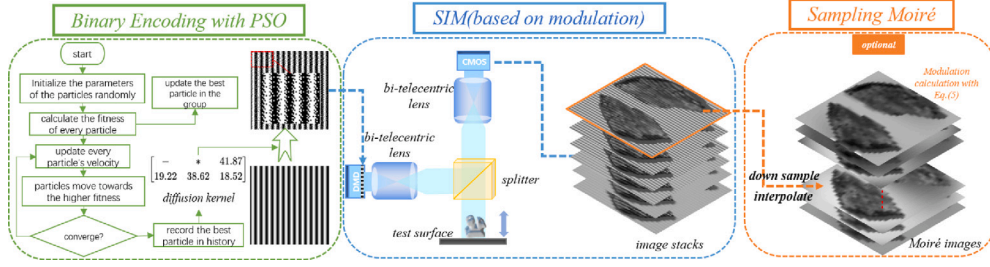


Fig. 1. The flowchart of the proposed method.

this work by incorporating an extra CCD camera to enhance reflectance disturbance resistance and measurement range. However, these methods sacrifice measurement range and increase system complexity with additional equipment. Other approaches minimize the number of projected fringes during scanning to reduce exposure time. Yang et al. used a “flying phase shift” strategy inspired by white light interferometry (WLI) in SIM, resulting in improved scanning speed [20]. However, this method has stricter requirements for scanning intervals. Chai [21] and Cheng [22] employed deep learning techniques to extract modulation information from a single fringe. While these methods greatly reduce the number of required images, they necessitate substantial training data, and the trained model is specific to the measuring system.

Binary-encoded fringe patterns are commonly used in digital fringe projection due to their robustness against dynamic surface characteristics, noise, and the non-linear response of digital video projectors [23]. These fringes exhibit sensitivity to defocus, which aligns well with the requirements of SIM [24]. The SM method, a vision-based non-contact deformation measurement technique, plays a crucial role in structural health monitoring and understanding material damage mechanisms [25–27]. With SM, we can decode modulation from a single fringe, which perfectly matches SIM’s goal of reducing the camera’s exposure time.

Our research introduces significant contributions that enhance imaging techniques and offer new possibilities in various fields. Firstly, we apply the Particle Swarm Optimization (PSO) to encode binary fringes. This encoding method increases the variance around the peak of AMR, enabling more accurate peak extraction. Secondly, we utilize SM to calculate modulation from a single fringe, greatly reducing exposure time. Thorough theoretical analysis and experimental verification on millimeter-scale samples validate the feasibility and effectiveness of this approach (Fig. 1).

## 2. Methodology

### 2.1. Modulation-based structure illumination microscopy

In geometrical optics, an object point is imaged as a point on the focal plane, dispersing as a diffuse circle in front of and behind it (Fig. 2(a)). Here,  $s$  stands for the object distance,  $z$  for the image distance, and  $f$  is the focal length of the lens. The imaging point is only focused when (1) is satisfied, coinciding with the peak of the AMR. The simulated AMR is shown in Fig. 2(b). To detect the focal position, methods such as the maximum point method, centroid algorithm, and polynomial curve fitting can be used. The maximum point and the centroid algorithm have lower accuracy than polynomial curve fitting [28]. In our approach, we utilize the centroid algorithm to determine the potential peak range, followed by polynomial curve fitting to precisely locate the peak. The centroid algorithm is presented in (2). This can reduce the amount of calculations required for polynomial fitting and speed up the process.

$$\frac{1}{f} = \frac{1}{s} + \frac{1}{z}. \quad (1)$$

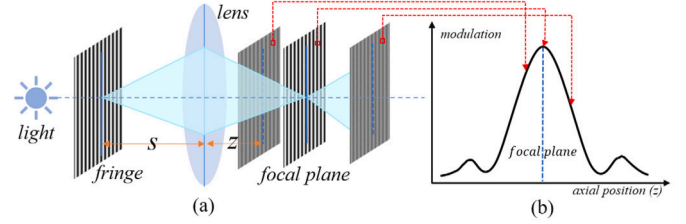


Fig. 2. The principle of SIM. (a) presents the captured fringes with a different focus and (b) shows the axial modulation response curve of a coordinate position.

$$CoG = \frac{\sum M_z * z}{\sum M_z}, \quad M_z = 0 \quad \text{if} \quad M_z \geq \frac{\max(M)}{2}. \quad (2)$$

Generally, the sinusoidal fringe can be denoted as

$$I(x, y) = I_0(x, y)[1 + C_0(x, y) \cos \varphi(x, y)], \quad (3)$$

where  $I_0$  is the background intensity,  $C_0$  describes the contrast of the fringe and  $\varphi(x, y)$  is the phase distribution. Phase shift and FT are commonly used methods for analyzing modulation. Phase shift involves projecting and capturing multiple fringes with a specific phase relationship, while FT only requires a single fringe to meet the requirements. However, the accuracy of FT is lower compared to phase shift. For example, in the  $N$ -step phase shift, the  $n$ th projected fringes can be represented as follows.

$$I_n(x, y) = I_0(x, y) (1 + C_0(x, y) \cos(\varphi(x, y) + 2\pi n/N)), \quad (4)$$

$(N = 1, 2, 3, \dots, N).$

The modulation of the fringes,  $M(x, y)$ , is proportional to the contrast of the fringes,  $C_0(x, y)$ , with a scale factor of  $NI_0(x, y)/2$ . It is defined as

$$M(x, y) = \sqrt{\left[ \sum_{n=0}^{N-1} I_n(x, y) \sin(2\pi n/N) \right]^2 + \left[ \sum_{n=0}^{N-1} I_n(x, y) \cos(2\pi n/N) \right]^2}. \quad (5)$$

Different from the phase shift method, FT obtains the result of (6) by performing FT on (3)

$$G(f_x, f_y) = G_0(f_x, f_y) + G_1(f_x, f_y) + G_{-1}(f_x, f_y). \quad (6)$$

$G_0$  represents the zero-frequency component of the Fourier spectrum, while  $G_1$  and  $G_{-1}$  represent the symmetrical frequency components that are required.

$$B(x, y) = 1/2 I_0(x, y) C_0(x, y) \exp(i\varphi(x, y)). \quad (7)$$

The modulus of  $B(x, y)$  represents the fringe modulation, which is directly related to the contrast of the fringes,  $C_0(x, y)$ , with a scale factor of  $I_0(x, y)/2$ . Although the scaling factor differs from that of the phase shift method, it does not alter the distributional properties of the modulation in the  $Z$ -direction.

## 2.2. Binary encoded fringe

The current SIM technique utilizes sinusoidal fringes for measurement. However, sinusoidal fringes are less affected by minimal defocus, leading to slight variations in modulation near the peak of the AMR curve. This sensitivity to noise interference hampers the accuracy of the fitting. On the other hand, binary fringes demonstrate significant variations near the peak due to their inclusion of high-frequency components and high sensitivity to defocus. To explore this further, we simulate lens defocus effects using Gauss filtering. First, we convert the familiar spatial domain Gauss filtering to the frequency domain. We illustrate this using a one-dimensional Gauss distribution to simplify the expression. The one-dimensional Gauss function in space is expressed as (8) and its FT form is as (9). The appendix contains a comprehensive derivation of (9).

$$f(x) = \frac{1}{\sqrt{2\pi}\sigma} e^{-\frac{x^2}{2\sigma^2}}. \quad (8)$$

$$\begin{aligned} F(\omega) &= \int_{-\infty}^{+\infty} f(x) e^{-j\omega x} dx, (\omega = 2\pi\mu) \\ &= \int_{-\infty}^{+\infty} \left( \frac{1}{\sqrt{2\pi}\sigma} \right) e^{-\frac{x^2}{2\sigma^2}} e^{-j\omega x} dx \\ &= e^{-\frac{\mu^2}{2\sigma^2}} \end{aligned} \quad (9)$$

The FT of the Gauss function is still a Gauss function, as shown by (9). The Gauss window ( $\sigma$ ) in the spatial domain grows wider as defocus rises, whereas the Gauss window in the frequency domain narrows in contrast. In the case of sinusoidal fringes, there is only one frequency present, and it remains unaffected until the Gauss window in the frequency domain becomes sufficiently narrow. To enhance the modulation variation around the focal plane, we need to encode the fringe with additional high-frequency components. Conversely, when encoding the binary fringe, we should aim for a similar representation as the sinusoidal fringe to minimize errors in modulation calculation with (5).

Inspired by [29], PSO is used to optimize the error diffusion kernel [30] for the binary coding of sinusoidal fringes. The formula for error diffusion coding is (10) and (11). We combine intensity and frequency error in slight out-of-focus as the PSO error function, as indicated in (12). By doing so, we can minimize modulation errors through subtle Gauss filtering while retaining essential high-frequency components to enhance the sharpness of the AMR peak.

$$I_b(i, j) = \text{binarize}(I_s(i, j) + \sum_i \sum_j \text{Kernel}(x, y) e(i - x, j - y)). \quad (10)$$

$$\text{Kernel} = \frac{1}{\sum_{i=1}^4 \omega_i} \begin{bmatrix} - & * & \omega_1 \\ \omega_2 & \omega_3 & \omega_4 \end{bmatrix}. \quad (11)$$

$I_b$  is the binary fringe encoded with an error diffusion kernel and  $I_s$  is the sinusoidal fringe. The kernel parameters are solved with PSO.

$$\begin{cases} E = E_i + E_f \\ E_i = \sqrt{\frac{\sum (I_b \otimes G - I_s)^2}{N-1}} \\ E_f = \sqrt{\frac{\sum (F(I_b \otimes G) - F(I_s))^2}{N-1}} \end{cases} \quad (12)$$

$N$  is the pixels of the fringe, and  $F$  denotes the 2D FT.  $G$  is the  $3 \times 3$  Gauss kernel and  $\otimes$  indicates the convolution operation.

In the PSO algorithm, the kernel parameters  $\omega_i$  are determined by the particle positions within the group, while their fitness is indicated by  $1/E$ . In each iteration, particles adjust their positions by moving towards the best particle in the group and the historical best position, with

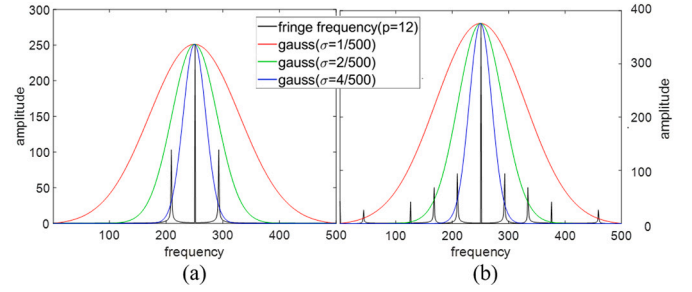


Fig. 3. The impact of various Gauss windows (a) on sinusoidal fringes, and (b) on binary encoded fringes.

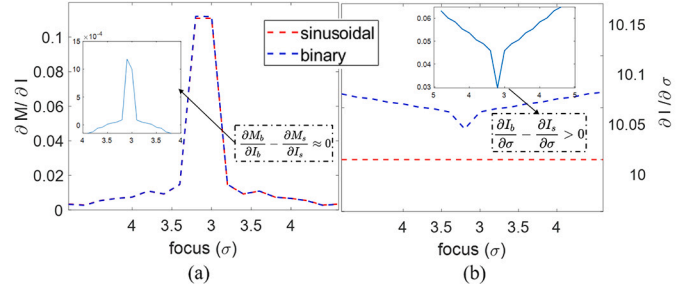


Fig. 4. The trend of partial derivatives of sinusoidal and binary encoded fringes with defocus. (a) presents the trend of  $\frac{\partial M}{\partial I}$ , and (b) is about  $\frac{\partial I}{\partial \sigma}$ .

some randomness considered. For a fringe period of 12, the calculated kernel parameters are as follows:  $\omega_1 = 41.87$ ,  $\omega_2 = 19.22$ ,  $\omega_3 = 38.62$ , and  $\omega_4 = 18.52$ .

Fig. 3(a) and (b) depict the influence of different Gauss windows on sinusoidal and binary encoded fringes, respectively. Increasing defocus (indicated by a larger  $\sigma$  value) causes a rapid reduction in high-frequency components in the binary encoded fringes (Fig. 3(b)), leading to a sharp decrease in image intensity ( $I_b$ ). However, the sinusoidal fringe remains unaffected until  $\sigma$  reaches a sufficiently large value, maintaining a relatively constant intensity ( $I_s$ ). Thus, it can be concluded that  $\frac{\partial I_b}{\partial \sigma} > \frac{\partial I_s}{\partial \sigma}$ . By calculating modulation using equation (5),  $\frac{\partial M_s}{\partial I_s} \approx \frac{\partial M_b}{\partial I_b}$  since the fringes share the same phase shift. Consequently, employing the chain rule for derivatives,  $\frac{\partial M}{\partial \sigma} = \frac{\partial M}{\partial I} \times \frac{\partial I}{\partial \sigma}$ , we can infer that  $\frac{\partial M_b}{\partial \sigma} > \frac{\partial M_s}{\partial \sigma}$ , suggesting that the binary fringe's modulation is more sensitive to defocus.

We perform simulations of the defocusing process with SIM scanning using the “imgaussfilt(A, sigma)” function in Matlab, and then calculate the values of the partial derivatives,  $\frac{\partial M}{\partial I}$  and  $\frac{\partial I}{\partial \sigma}$ , for both types of fringes at various levels of defocus. The results are shown in Fig. 4. It can be observed that the partial derivative  $\frac{\partial M}{\partial I}$  for binary encoded fringes is similar to that of sinusoidal fringes in Fig. 4(a). However, the fluctuations of  $I_s$  in Fig. 4(b) are minimal, and  $\frac{\partial I_b}{\partial \sigma}$  is larger than  $\frac{\partial I_s}{\partial \sigma}$ .

## 2.3. Sampling Moiré

We obtain the Moiré fringes, following the downsampling and intensity interpolation steps. Subsequently, the SM technique applies a phase shift operation to extract both the modulation and phase information from these Moiré fringes. Fig. 5 illustrates the process of SM. Qian and his team discussed SM as a special kind of windowed Fourier ridge (WFR) in [31] and verified that both SM and WFR outperform the 2D FT, which is always utilized in SIM for single-shot fringe analysis [32]. Theoretically, when the sampling interval is appropriately selected, the SM method can decode the modulation from a single image with minimal to no errors, instead of scanning for searches as WFR does [31]. Therefore, we employ the SM technique to solve the modulation from a single-shot fringe efficiently.

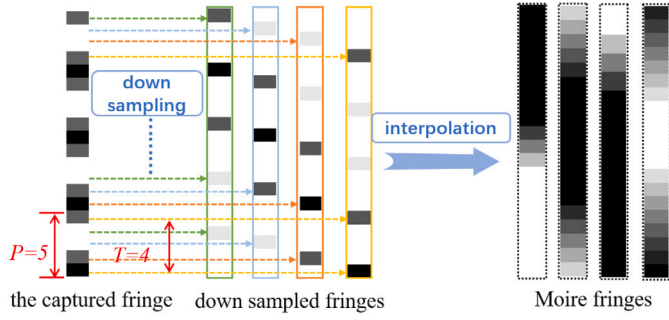


Fig. 5. The theory of SM, the period of original fringe  $P$  is 5 and the sampling interval  $T$  equals 4.

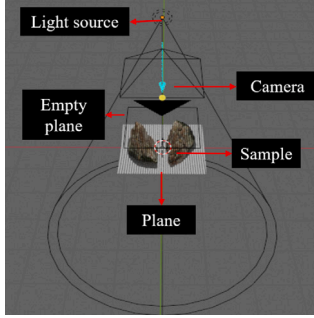


Fig. 6. Simulation environment in Blender 3.0.0.

The captured fringe can be written as (13).

$$I(x, y) = a \cos\left(\frac{2\pi x}{p} + \varphi_0\right) + b. \quad (13)$$

$b$  denotes the background intensity,  $c = a/b$  is the contrast of the fringe,  $p$  symbolizes the period of the fringe and  $\varphi_0$  indicates the phase shift. The images obtained after downsampling at interval  $T$  are represented in (14), and the Moiré fringes obtained after linear interpolation are shown in (15).  $k$  denotes the  $k$ th sampling frame, and  $l$  is the position between each interpolation interval. Shien et al. [33] have rigorously proved that when  $T = p$ , the modulation of the Moiré fringes is also proportional to the original fringe contrast  $c$ .

$$f(x, y; k) = a \cos\left[2\pi x\left(\frac{1}{p} - \frac{1}{T}\right) + \frac{2\pi k}{T} + \varphi_0\right]. \quad (14)$$

$$I_m(x, y; k) = \frac{1}{T}[(T-l) \cdot f(x-l, y; k) + l \cdot f(x-l+T, y; k)] \quad (15)$$

$$k = (0, 1, \dots, T-1), l = (x-k) \bmod T.$$

### 3. Simulations

Simulation experiments are conducted using the open-source 3D rendering tool Blender 3.0.0, known for its accurate simulation of real scenes [34,35]. The experimental setup, shown in Fig. 6, involves a spotlight source as the projector and an orthographic camera model to simulate bi-telecentric imaging. The camera's aperture has an F-stop of 3.8, a ratio of 1.0, and an image resolution of  $1000 \times 1000$  pixels. By adjusting the empty plane's position, various defocus levels can be achieved. Additionally, a sunlight source is incorporated to simulate environmental disturbances.

We begin by independently validating the accuracy of binary-encoded fringes through measurements on a flat plane. Therefore SM as a windowed Fourier filter is not applied in this process, we obtain modulation results with the 5-step phase shift algorithm, instead. We capture data from a plane using two types of fringes: sinusoidal fringes and binary-encoded fringes. The modulations are obtained with a 5-step phase shift algorithm. Fig. 7 presents the reconstructed plane using

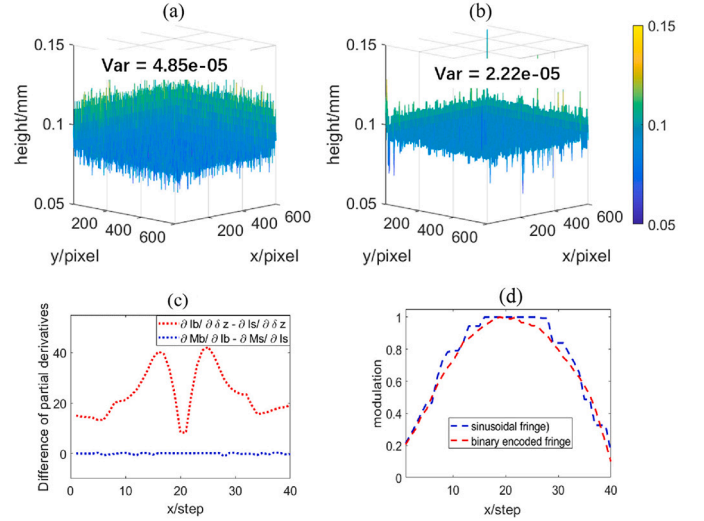


Fig. 7. The plane is measured using (a) sinusoidal fringes and (b) binary-encoded fringes. In (c), the blue dashed line represents  $\frac{\partial M_b}{\partial I_b} - \frac{\partial M_s}{\partial I_s}$ , which approaches zero, while the red line indicates  $\frac{\partial I_b}{\partial x} - \frac{\partial I_s}{\partial x}$ , which is greater than zero. (d) compares the AMR of the two fringe types at the same coordinate position, reflecting the change in scanning step  $x$  corresponding to the defocus window  $\sigma$ .

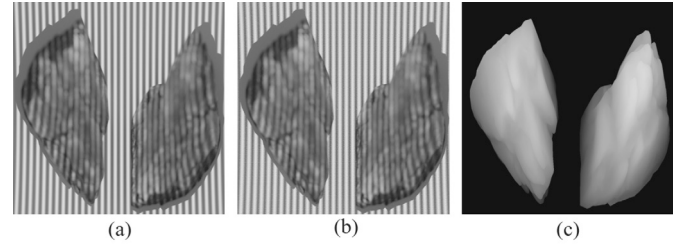


Fig. 8. The images are captured when (a) sinusoidal fringes, and (b) binary fringes are projected. (c) the depth map of the stone.

both fringe types, with labeled variances for each reconstructed plane. In Fig. 7(b), high-frequency components introduce local outliers. However, the variance in (b) is significantly reduced by more than 20% compared to (a), indicating improved accuracy. Additionally, Fig. 7(c) displays the trends of  $\frac{\partial M_b}{\partial I_b} - \frac{\partial M_s}{\partial I_s}$  and  $\frac{\partial I_b}{\partial x} - \frac{\partial I_s}{\partial x}$  during the scanning process. It is evident that  $\frac{\partial M_b}{\partial I_b} \approx \frac{\partial M_s}{\partial I_s}$  and  $\frac{\partial I_b}{\partial x} > \frac{\partial I_s}{\partial x}$ , aligning with Sec. 2.2. Furthermore, Fig. 7(d) illustrates the distinct AMRs exhibited by the two fringe types. The peak variances of binary-encoded fringes surpasses sinusoidal fringes, providing a plausible explanation for the higher accuracy achieved using binary-encoded fringes.

In addition, we conduct measurements on a sample that exhibits a complex texture, introducing additional disturbances to validate the efficiency and effectiveness of the SM technique, as can be seen in Fig. 8. The obtained results are visually presented in Fig. 9, where the root mean square error (RMSE) of the three topographies is calculated and displayed in white boxes. All RMSEs are calculated by comparing the measurements obtained from the respective methods with the actual height of the samples. Considering the edge effect of the Fourier transform, we retain the edge region when calculating the region of interest (equivalent to padding the data) and then exclude the edge data when analyzing the results to ensure a fair comparison in depth calculation. This treatment is applied consistently throughout the subsequent experimental analysis.

In Fig. 10, three lines of different heights (red, green, and blue) are shown within the context of Fig. 9 for clarity. The results indicate that the SM method effectively preserves the sample's shape, demonstrating



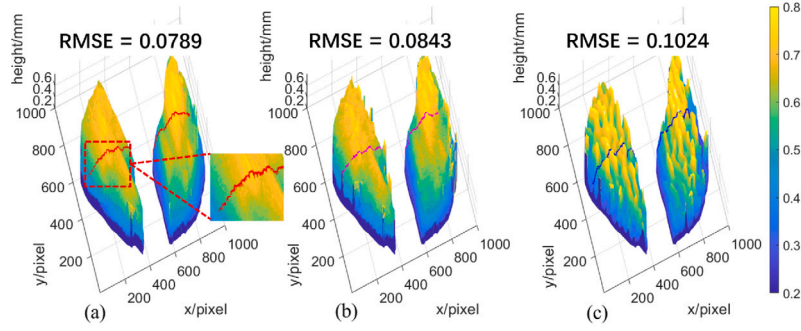


Fig. 9. The reconstructed sample with (a) the 5-step phase shift, (b) SM, and (c) FT when binary-encoded fringes are projected.

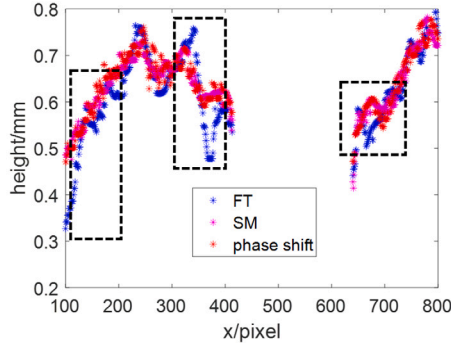


Fig. 10. A single line of the sample height is measured with (a) the 5-step phase shift, (b) SM, and (c) FT. The measured result of the FT deviates from the phase-shifting result in black dashed boxes.

Table 1  
RMSE results of the sample in simulation.  
Units: mm.

B-5 phase shift	B-SM	B-FT
<b>0.0789</b>	<b>0.0843</b>	0.1024
S-5 phase shift	S-SM	S-FT
0.0852	<b>0.0843</b>	0.0943

its robustness in retaining essential features with a single-shot capture at each scanning position. This approach reduces the exposure time by 80%. Conversely, the FT method tends to oversmooth the modulation, resulting in a notable 28% increase in RMSE error.

$$RMSE = \sqrt{\frac{\sum_{m=1}^M \sum_{n=1}^N (D_1(m, n) - D_2(m, n))^2}{N \times M}}. \quad (16)$$

$M$  and  $N$  represent the width and height of the topography image separately.  $H$  is the depth map.

Ablation experiments were conducted using sinusoidal fringes and three modulation calculations, as illustrated in Fig. 11. The summarized results are presented in Table 1, where B represents binary fringes and S represents sinusoidal fringes. A comparison between Fig. 9(a) and Fig. 11(a) reveals that the reconstruction using sinusoidal fringes exhibits more surface error points. Table 1 demonstrates a 7.3% accuracy improvement with binary-encoded fringes, further confirming its effectiveness. Additionally, the ablation experiment results indicate that SM reduces camera exposure time and outperforms FT measurements under similar conditions, despite a compromise in accuracy.

#### 4. Experiments

To enhance the credibility and validity of our methodology, we perform physical measurements using a setup illustrated in Fig. 12.

Table 2  
RMSE of sample recovered with different methods.  
Units: mm.

the stage 1	B-5 phase shift	B-SM	B-FT
	<b>0.0222</b>	<b>0.0168</b>	0.0912
	S-5 phase shift	S-SM	S-FT
	0.0247	<b>0.0171</b>	0.1211
the stage 2	B-5 phase shift	B-SM	B-FT
	<b>0.0262</b>	<b>0.0260</b>	0.1452
	S-5 phase shift	S-SM	S-FT
	0.0276	<b>0.0260</b>	0.1408

The measurement system consists of a bi-telecentric camera, an electric translation stage (OptoSigma OSMS80-20ZF-0B), a splitter, and a bi-telecentric projector. For precise positioning, we employ the electric translation stage with a resolution of  $0.1 \mu\text{m}/\text{pulse}$ . To ensure accurate image acquisition, we use the Daheng MER2-301-125U3M camera ( $2048 \times 1536$  resolution) with the bi-telecentric lens WWH20-110AT-G, crucial for capturing high-quality images. Our setup utilizes a Texas Instruments DLP4500 chip projector known for excellent projection capabilities, paired with the bi-telecentric lens LDWH1X65-11C to achieve precise and uniform projection of patterns onto the target surface.

The reconstructed planes using both fringe types are shown in Fig. 13, along with the corresponding variance indicating reconstruction quality. Comparing Fig. 13(a) and Fig. 13(b), we observe an approximate 20% reduction in variation with binary-encoded fringes, aligning with simulation results. Fig. 13(c) displays the variations of  $\frac{\partial M_b}{\partial I_b} - \frac{\partial M_s}{\partial I_s}$  and  $\frac{\partial I_b}{\partial x} - \frac{\partial I_s}{\partial x}$  during the scanning process. Despite fluctuations,  $\frac{\partial M_b}{\partial I_b} \approx \frac{\partial M_s}{\partial I_s}$  and  $\frac{\partial I_b}{\partial x} - \frac{\partial I_s}{\partial x} > 0$  hold true for most of the scanning process. Fig. 13(d) illustrates the amplitude modulation response (AMR) of the two fringe types. The presence of noise significantly affects the AMR peak of sinusoidal fringes, highlighting the detrimental impact of noise on their accuracy. Our experimental results successfully confirm the reliability of binary-encoded fringes for precise surface reconstruction.

Subsequently, measurements were performed on two stepped objects with known heights, resulting in two sets of fringe images shown in Fig. 14. The modulation of sinusoidal and binary fringes was calculated using the 5-step phase shift, SM, and FT methods. It is worth noting that FT and SM methods utilize only one of the five phase-shifted images for modulation calculation.

Fig. 15 and 16 present the reconstructed results of the two stages. Comparing (b) and (c) in both figures, the FT approach exhibits noticeable inaccuracies, particularly along the edges. Conversely, the SM method provides more stable and closely aligned reconstructions to those obtained using the 5-step phase shift method.

Table 2 presents the RMSE values of the measured results, with B representing binary fringes and S representing sinusoidal fringes. The

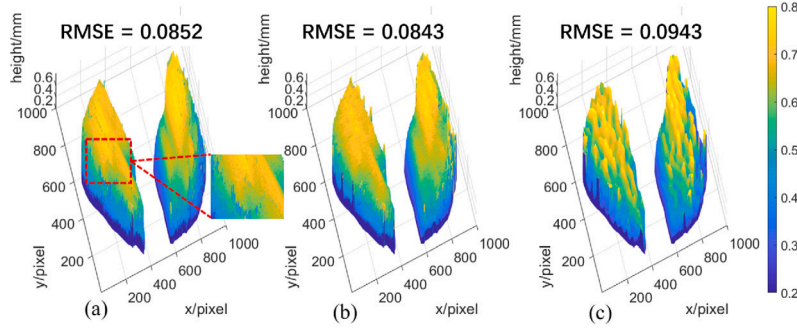


Fig. 11. The reconstructed sample with (a) the 5-step phase shift, (b) SM, and (c) FT when sinusoidal fringes are projected.

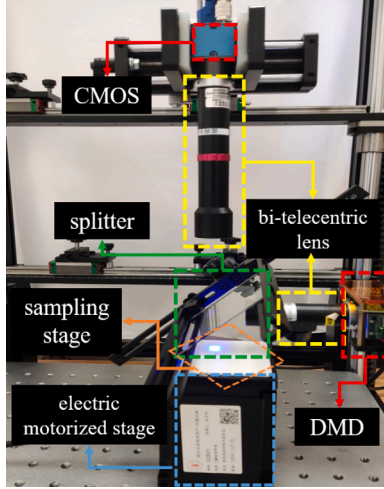


Fig. 12. The system setup.

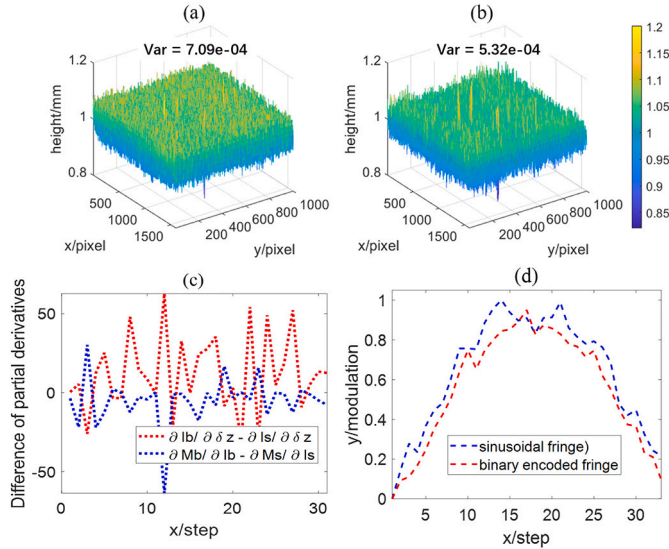


Fig. 13. The plane is reconstructed with (a) sinusoidal fringes, and (b) binary encoded fringes. In (c), the blue dashed line denotes  $\frac{\partial I_b}{\partial I_b} - \frac{\partial I_s}{\partial I_s}$ , which is close to 0 and the red one indicates  $\frac{\partial I_b}{\partial I_b} - \frac{\partial I_s}{\partial I_s}$  that is greater than 0. (d) compares the AMR of the two types of fringes in the same coordinate position. The change in the scanning step  $x$  represents the change in the defocus window  $\sigma$ .

table shows that binary fringes yield better measurement accuracy, with an improvement of 5-10% compared to sinusoidal fringes. Notably, the SM method even surpasses the accuracy of the 5-step phase shift due to its superior localized smoothing effect. When compared to the FT ap-

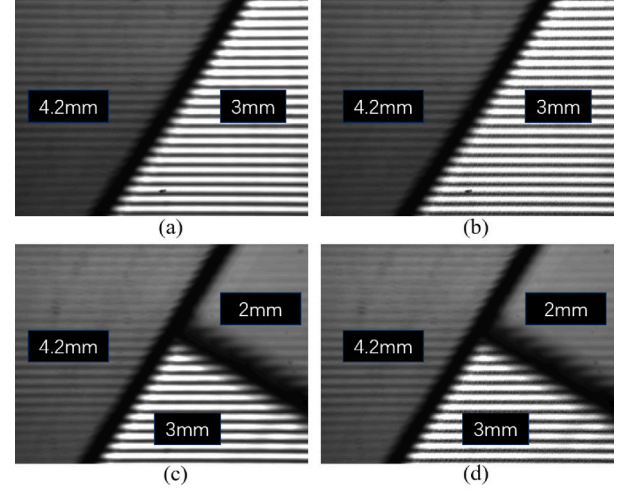


Fig. 14. The fringes captured from the measured objects are displayed in (a) and (b) for stage 1, and (c) and (d) for stage 2. The left two images correspond to the projection of sinusoidal fringes, while the right two images correspond to the projection of binary fringes.

proach, the SM method achieves an order of magnitude improvement in accuracy. This reduction in errors validates the reliability and effectiveness of the SM technique. These results confirm that binary-encoded fringes enhance accuracy, while the SM technique significantly reduces exposure time to 1/5 compared to the 5-step phase shift method while maintaining measurement precision.

## 5. Conclusion

In conclusion, our research has made significant advancements in 3D inspection through the application of SIM. By using binary-encoded fringes and the SM technique, we have improved the speed and accuracy of the process separately. The use of binary-encoded fringes has enhanced the precision of peak extraction, resulting in more accurate measurements. The SM technique has reduced the number of required fringes and improved the efficiency of capturing fringe modulation in a single shot. This has saved time and made the process more efficient. The topography reconstructed using the SM technique has demonstrated improved stability and accuracy compared to the FT method. Although SM can effectively reduce exposure time, it inevitably incurs a trade-off in measurement accuracy. Therefore, there exists a trade-off between utilizing SM to accelerate measurements in practice and maintaining optimal accuracy.

## Funding

This work was supported by the National Natural Science Foundation of China (grant number 62101364, 61901287); Sichuan Provincial

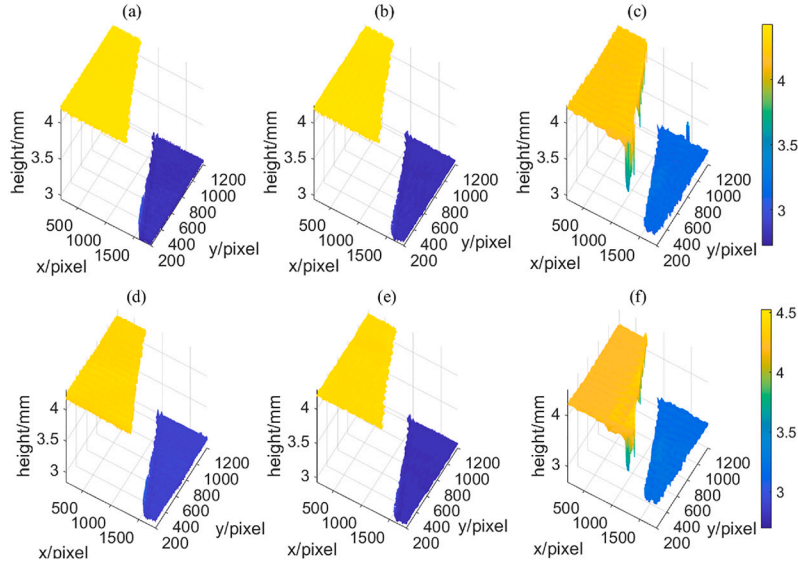


**Fig. 15.** The reconstructed stage 1 consists of three depth maps constructed using binary fringes (shown above) and three results constructed using sinusoidal fringes (shown below). The depth maps (a) and (d) are decoded using a 5-step phase shift, (b) and (e) are recovered using SM, and (c) and (f) are reconstructed using FT.

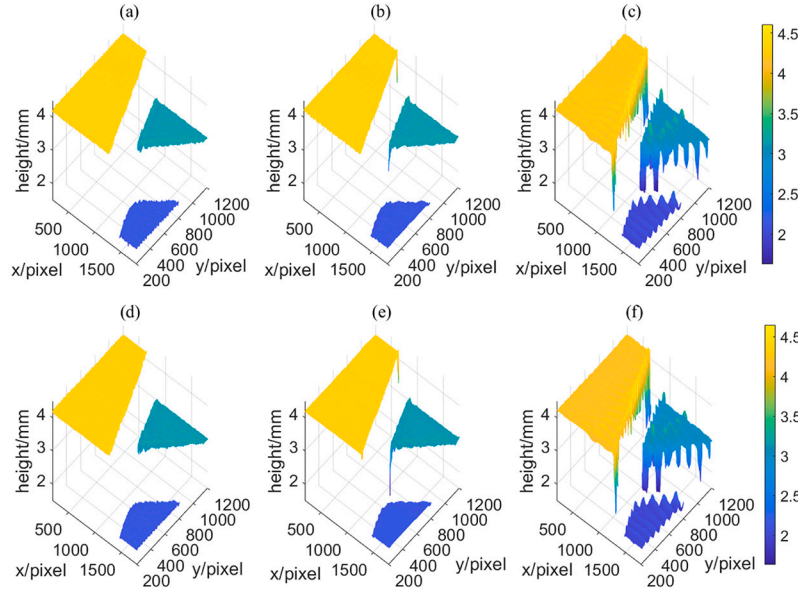


**Fig. 16.** The reconstructed stage 2 consists of three depth maps constructed using binary fringes (shown above) and three results constructed using sinusoidal fringes (shown below). The depth maps (a) and (d) are decoded using a 5-step phase shift, (b) and (e) are recovered using SM, and (c) and (f) are reconstructed using FT.

Central Guidance Local Science and Technology Development Project (2022ZYD0111); Key Research and Development Project of Sichuan Province (grant numbers 2022YFG0053); China Postdoctoral Science Foundation (2021M692260).

#### CRediT authorship contribution statement

**Zhoumiao He:** Visualization, Software, Methodology, Investigation, Conceptualization. **Pei Zhou:** Writing – review & editing, Validation. **Jianwei Zhang:** Supervision, Project administration. **Jiangping Zhu:** Resources, Methodology.

#### Declaration of competing interest

The authors declare that they have no known competing financial interests or personal relationships that could have appeared to influence the work reported in this paper.

#### Data availability

Data presented in this paper and the code will be uploaded to GitHub at <https://github.com/abaowannasleep/structured-illumination-microscopy>.

#### Appendix A. Derivation of (9)

$$F(\omega) = \int_{-\infty}^{+\infty} \left( \frac{1}{\sqrt{a\pi\sigma}} \right) e^{-\frac{1}{2\sigma^2}x^2} e^{-j\omega x} dx. \quad (\text{A.1})$$

Set  $a = \frac{1}{2\sigma^2}$ , (A.1) can be rewritten as

$$F(\omega) = \left( \frac{1}{\sqrt{a\pi\sigma}} \right) \int_{-\infty}^{+\infty} e^{-(ax^2 + j\omega x)} dx. \quad (\text{A.2})$$



Then, we have (A.3), and by substituting  $a = \frac{1}{2\sigma^2}$  into it, we obtain final result.

$$\begin{aligned}
 F(\omega) &= \left(\frac{1}{\sqrt{a\pi\sigma}}\right) \int_{-\infty}^{+\infty} e^{-\left(\sqrt{ax} + \frac{j\omega}{2\sqrt{a}}\right)^2} \cdot e^{\frac{(j\omega)^2}{2\sqrt{a}}} dx \\
 &= \left(\frac{1}{\sqrt{a\pi\sigma}}\right) e^{-\frac{\omega^2}{4a}} \int_{-\infty}^{+\infty} e^{-\left(\sqrt{ax} + \frac{j\omega}{2\sqrt{a}}\right)^2} dx \\
 &= \left(\frac{1}{\sqrt{a\pi\sigma}}\right) \sqrt{\frac{\pi}{a}} e^{-\frac{\omega^2}{4a}} = e^{-\frac{\mu^2}{2\pi^2\sigma^2}}.
 \end{aligned} \tag{A.3}$$

## Appendix B. Analysis time comparison

After optimization, we calculated the average analysis time per image 40 times. The image size is 1000\*1000 and the molar sampling period (P) is taken as 12, 24, 32, 48, 64 contrast Fourier transform with the 5-step phase shift method. The program runs on the regular personal computer and the software we adopted is matlabR2021a. Although sampled Moiré causes longer data post-processing time, the measurement time can be reduced by synchronizing sampling, transmission, and processing. However, there is no doubt, that it is possible to shorten the exposure time for sampling and thus achieve rapid data acquisition (Table B.3).

**Table B.3**

Analysis time of each image with different methods. Units: s.

FT	5-step PS	SM(P = 12)	SM(P = 24)	SM(P = 36)	SM(P = 48)
0.0378	0.0356	0.6758	1.3466	1.7890	2.6735

## References

- [1] Bochenek B, Pyrz R. Reconstruction of random microstructures—a stochastic optimization problem. *Comput Mater Sci* 2004;31:93–112.
- [2] Tahmasebi P. Accurate modeling and evaluation of microstructures in complex materials. *Phys Rev E* 2018;97:023307.
- [3] Meng W, Quanyao H, Yongkai Y, Yang Y, Qijian T, Xiang P, et al. Large dof microscopic fringe projection profilometry with a coaxial light-field structure. *Opt Express* 2022;30:8015–26.
- [4] Smith CL. Basic confocal microscopy. *Curr Protoc Neurosci* 2011;56:2.
- [5] Deng Q, Liu J, Tang Y, Zhou Y, Yang Y, Li J, et al. Spatial modulation-assisted scanning white-light interferometry for noise suppression. *IEEE Photonics Technol Lett* 2017;30:379–82.
- [6] Häusler G, Richter C, Leitz K-H, Knauer MC. Microdeflectometry—a novel tool to acquire three-dimensional microtopography with nanometer height resolution. *Opt Lett* 2008;33:396–8.
- [7] Saxena M, Eluru G, Gorthi SS. Structured illumination microscopy. *Adv Opt Photonics* 2015;7:241–75.
- [8] Křížek P, Raška I, Hagen GM. Flexible structured illumination microscope with a programmable illumination array. *Opt Express* 2012;20:24585–99.
- [9] Wang H, Tan J, Liu C, Liu J, Li Y. Wide-field profiling of smooth steep surfaces by structured illumination. *Opt Commun* 2016;366:241–7.
- [10] Neil MA, Juškaitis R, Wilson T. Method of obtaining optical sectioning by using structured light in a conventional microscope. *Opt Lett* 1997;22:1905–7.
- [11] Takeda M, Ina H, Kobayashi S. Fourier-transform method of fringe-pattern analysis for computer-based topography and interferometry. *J Opt Soc Am* 1982;72:156–60.
- [12] Vogel M, Kessel A, Yang Z, Faber C, Seraphim M, Häusler G. Tuning structured illumination microscopy (sim) for the inspection of micro optical components. In: *Proc. DGAO*, vol. 111; 2010. p. A22.
- [13] Vogel M, Yang Z, Kessel A, Kranitzky C, Faber C, Häusler G. Structured-illumination microscopy on technical surfaces: 3d metrology with nanometer sensitivity. In: *Optical measurement systems for industrial inspection VII*, vol. 8082. SPIE; 2011. p. 245–50.
- [14] Yang Z, Kessel A, Häusler G. Better 3d inspection with structured illumination: signal formation and precision. *Appl Opt* 2015;54:6652–60.
- [15] Yan H, Chai C, Du X, Liu X. The modified weighted Gauss-fitting algorithm for structured-illumination microscopy. In: *2021 IEEE 5th information technology, networking, electronic and automation control conference (ITNEC)*, vol. 5. IEEE; 2021. p. 1–5.
- [16] Lee C-H, Mong H-Y, Lin W-C. Noninterferometric wide-field optical profilometry with nanometer depth resolution. *Opt Lett* 2002;27:1773–5.
- [17] Lu M, Su X. Vertical measurement method for structured light three-dimensional profilometry based on phase-shifting and modulation ratio. *Chin J Lasers* 2019;46:0704003.
- [18] Xie Z, Tang Y, Feng J, Liu J, Hu S. Accurate surface profilometry using differential optical sectioning microscopy with structured illumination. *Opt Express* 2019;27:11721–33.
- [19] Han C, Tang Y, Xie Z, Liu L, Feng J, Hu S. Fast structured illumination microscopy with a large dynamic measurement range. *Appl Opt* 2021;60:5169–76.
- [20] Yang Z, Bielke A, Häusler G. Better three-dimensional inspection with structured illumination: speed. *Appl Opt* 2016;55:1713–9.
- [21] Chai C, Chen C, Liu X, Lei Z. Deep learning based one-shot optically-sectioned structured illumination microscopy for surface measurement. *Opt Express* 2021;29:4010–21.
- [22] Cheng X, Tang Y, Yang K, Liu L, Han C. Single-exposure height-recovery structured illumination microscopy based on deep learning. *Opt Lett* 2022;47:3832–5.
- [23] Geng J. Structured-light 3d surface imaging: a tutorial. *Adv Opt Photonics* 2011;3:128–60.
- [24] Kamagata A, Wang X, Li S. Optimal defocus selection based on normed Fourier transform for digital fringe pattern profilometry. *Appl Opt* 2017;56:8014–22.
- [25] Ri S, Fujigaki M, Morimoto Y. Sampling Moiré method for accurate small deformation distribution measurement. *Exp Mech* 2010;50:501–8.
- [26] Morimoto Y, Fujigaki M, Masaya A, Kondo H, Inuzuka T. Accurate displacement measurement for landslide prediction by sampling Moiré method. *Adv Mater Res* 2009;79:1731–4.
- [27] Wang Q, Ri S. Sampling Moiré method for full-field deformation measurement: a brief review. *Theor Appl Mech Lett* 2022;12:100327.
- [28] Xie Z, Tang Y, Zhou Y, Deng Q. Surface and thickness measurement of transparent thin-film layers utilizing modulation-based structured-illumination microscopy. *Opt Express* 2018;26:2944–53.
- [29] Zhu J, Luo J, Du J, Zhou P. Spatial-temporal binarization method via jointly optimizing diffusion kernel and quantization threshold for 3-d surface imaging. *IEEE Trans Instrum Meas* 2024;73:1–13. <https://doi.org/10.1109/TIM.2024.3364260>.
- [30] Floyd RW. An adaptive algorithm for spatial gray-scale. *Proc Soc Inf Disp* 1976;17:75–7.
- [31] Kemao Q, Agarwal N, Ri S, Wang Q. Sampling Moiré as a special windowed Fourier ridges algorithm in demodulation of carrier fringe patterns. *Opt Eng* 2018;57:100503.
- [32] Ri S, Agarwal N, Wang Q, Kemao Q. Comparative study of sampling Moiré and windowed Fourier transform techniques for demodulation of a single-fringe pattern. *Appl Opt* 2018;57:10402–11.
- [33] Ri S, Muramatsu T. Theoretical error analysis of the sampling Moiré method and phase compensation methodology for single-shot phase analysis. *Appl Opt* 2012;51:3214–23.
- [34] Zheng Y, Wang S, Li Q, Li B. Fringe projection profilometry by conducting deep learning from its digital twin. *Opt Express* 2020;28:36568–83.
- [35] He Z, Zhou P, Zhu J, Zhang J. Improved shape-from-focus reconstruction for high dynamic range freedom surface. *Opt Lasers Eng* 2023;170:107784.